Glucocorticoid signaling delays castration-induced regression in murine models of prostate cancer

Aerken Maolake[1], Renyuan Zhang[1], Kai Sha[1], Shalini Singh[1], Chunliu Pan[1], Bo Xu[2], Gurkamal Chatta[3], Michalis Mastri[1], Kevin H. Eng[1,4], Kent L. Nastiuk[1,5 *] and John J. Krolewski[1 *]

[1]Departments of Cancer Genetics and Genomics, [2]Pathology and Laboratory Medicine, [3]Medicine, [4]Biostatistics & Bioinformatics and [5]Urology

Roswell Park Comprehensive Cancer Center

Buffalo, NY 14263

***CO-CORRESPONDING AUTHORS:**

J.J. Krolewski, Department of Cancer Genetics and Genomics; Elm and Carlton Streets; Buffalo, NY 14263; john.krolewski@roswellpark.org; 716-845-8964

K.L. Nastiuk, Department of Cancer Genetics and Genomics; Elm and Carlton Streets; Buffalo, NY 14263; kent.nastiuk@roswellpark.org; 716-845-5771

KEY WORDS: prostate cancer, castration, regression, high-frequency ultrasound imaging, glucocorticoid receptor, PTEN, c-MYC

CONFLICTS OF INTEREST: The authors declare that there are no potential conflicts of interest.

FINANCIAL SUPPORT: This work was supported by the Department of Defense Prostate Cancer Research Program No. W81XWH-19-1-0378 (to J.J. Krolewski), institutional funds from the Roswell Park Alliance Foundation and the National Cancer Institute Cancer Center Support Grant P30-CA016056 to Roswell Park Comprehensive Cancer Center.

ABSTRACT

Androgen deprivation therapy (ADT) is the mainstay therapy for recurrent and advanced prostate cancer. While human prostate cancers initially regress following ADT, many tumors fail this therapy and recur. To understand the response of prostate cancers to ADT, we have employed high frequency ultrasound imaging to track the kinetics of tumor volume in murine models of prostate cancer. Previously, we showed that normal (non-tumor) prostate regression begins within two days of castration. Following castration, murine prostate cancers also regress but only after a delay of 3-14 days, dependent on initial tumor size. Delayed regression is observed in two distinct mouse models (MYC over-expression, PTEN-deficient) implying that the genetic lesion which initiates carcinogenesis does not play a role. Intra-tumoral androgen levels are undetectable 16 hours post-castration, arguing that residual androgen signaling is not the cause of delayed regression. Castration induces tumor cell proliferation during this period. There is an increase in the active glucocorticoids, as well as glucocorticoid receptor (GR) mRNA and protein and a set of GR-regulated genes. A selective GR inhibitor eliminates the delayed regression phenotype in both models. Thus, GR signaling is activated following castration and transiently enhances tumor proliferation. This response to ADT resembles the GR-dependent mechanism of escape for prostate cancers that are resistant to anti-androgen therapies and may provide mechanistic insight into the development of castration resistant prostate cancer. If ADT-induced GR signaling is similar in human prostate cancers, simultaneous blockade of GR and androgen receptor signaling could improve prostate cancer therapy.

INTRODUCTION

Prostate cancer (PC) is one of the more frequently diagnosed malignancies in U.S. men with 191,930 new diagnoses and 33,330 deaths in 2020 (1). While many tumors are indolent or can be eliminated by curative surgery or radiotherapy, PC that presents at an advanced stage, or that is recurrent or metastatic is difficult to treat and cure. These tumors eventually constitute the bulk of prostate cancer deaths (2). Although the precise etiology of PC remains uncertain, primary tumor growth is driven by the androgen receptor (AR) axis, via re-programming of the AR cistrome (3). The re-programmed AR cistrome is, in turn, dependent on the presence of circulating androgens, providing the rationale for androgen deprivation therapy (ADT). ADT has long been the mainstay therapy for PC. It is initially effective but most prostate cancers become resistant within a few years and PC progresses to castration-resistant prostate cancer (CRPC). Attempts to improve PC therapy by combining ADT with either chemotherapy, androgen biosynthesis inhibitors or AR-targeting anti-androgens are ongoing (4). Thus, improved understanding of the mechanism of tumor response to ADT may be valuable in interpreting the results of clinical trials.

To investigate the response of prostate cancers to ADT, we have employed two well-characterized genetically engineered murine models (GEMMs) of prostate cancer, driven by prostate-specific PTEN-loss or c-MYC gain, respectively (reviewed in ref. (5)). These genetic lesions are common in both primary and metastatic human prostate cancers, suggesting the corresponding mice are robust models of human prostate cancer. To optimize our understanding of tumor development and response to therapy, we have developed a protocol to serially image murine prostates using high frequency ultrasound (HFUS) in combination with software that enables three-dimensional reconstruction from the ultrasound image data (6). This relatively rapid and affordable methodology can accurately determine tumor size and location within the multi-lobed murine prostate and non-invasive serial imaging provides insight into the kinetics of tumor volume under various conditions or treatments. In this report, we demonstrate that castration causes the tumors in these murine models of prostate cancer to regress over a period of 4 weeks,

but that there is an initial delay in regression, relative to the effect of castration on the normal murine prostate (7). We combined molecular analyses with the use of a selective glucocorticoid receptor (GR) modulator (8) to demonstrate that delayed regression occurs because GR signaling transiently substitutes for AR signaling in the prostate cancers.

MATERIALS AND METHODS

Genetically engineered mouse prostate cancer models

Two genetically engineered mouse models of prostate cancer were breed in the Roswell Park Experimental Tumor Model shared resource, maintained on a 12-hour light, 12-hour dark cycle in a temperature and humidity controlled room with free access to food and water. PB-Cre x PTEN$^{fl/fl}$ mice (9) were generated by crossing male PB-Cre4 (Frederick Lab, NCI) and female PTEN$^{fl/fl}$ (Jackson Labs) mice. Transgenic ARR_2/probasin-*Myc* (Hi-MYC) mice (10) were from Frederick Lab, NCI. For both GEMMs, male pups were genotyped and monitored for tumor development by imaging (see below) beginning at 12 weeks. Mice were enrolled in experiments when tumors were >300 mm^3 and animals were older than 6 months age. Castration and imaging were performed using isoflurane anesthetic, as described previously (6). In some cases, mice received 20mg/kg/day intraperitoneal injections of CORT125281 (11), which was reconstituted at 40mg/ml in DMSO and further diluted with sesame oil. All animal studies were performed in accordance with the National Institute of Health Guidelines for the Care and Use of Laboratory Animals and Use of Laboratory Animals and approved by Roswell Park Institutional Animal Care and Use Committee (1308M).

Three-dimensional ultrasound imaging

Ultrasound imaging of prostate tumors was performed using a Vevo 2100 micro-ultrasound imaging system (Vevo LAZR; VisualSonics Inc., Toronto) with a 21-MHz linear-array transducer system (LZ250; 13-24 MHz maximal broadband frequency; 21 MHz center frequency, 75 μm axial resolution, 80 μm lateral resolution, 23 mm maximal lateral field of view) in the Roswell Park

Translational Imaging shared resource. Briefly, mice were anesthetized with isoflurane, the abdomen was depilated and ultrasound transmission gel was applied. Three-dimensional scans of ultrasound B-mode image being recorded digitally and 3D stacks of these B-mode images were imported into AMIRA software (Visualization Sciences Group, Burlington MA) for tumor volume reconstruction.

Steroid metabolite determinations

Roswell Park Bioanalytics, Metabolomics and Pharmacokinetics shared resource, using LC/MS/MS methodology, as previously described (12).

Histology and immunohistochemistry

Mouse prostate tumors were identified grossly, excised and fixed in 10% formaldehyde for two days, embedded in paraffin, and cut into 5 um sections onto glass slides. Individual sections were stained with hematoxylin and eosin (H&E) or immunohistochemically stained using an antibody to Ki67 (Abcam, cat. no. 15580; 1:1000), on an automated staining platform in the Roswell Park Experimental Tumor Model shared resource. Stained sections were viewed and photographed on an OLYMPUS BX45 microscope. In the case of Ki67 IHC, representative ROIs were identified and positive stained tumor cell nuclear were counted, and divided by the number of total tumor cell nuclei to generate a Ki67 index (% positive staining tumor nuclei).

Immunoblot analysis

Protein extracts were prepared by grinding frozen tissue with a pestle in a mortar containing liquid nitrogen. The resulting frozen powder was dissolved in lysis buffer, sonicated for 8 seconds at 10 watts and insoluble protein and debris were pelleted by high-speed centrifugation. Extracts from PTEN-deficient mouse tumors were prepared in a 1% SDS lysis buffer (1% SDS, 20mM Tris-HCl pH7.5, 150mM NaCl, 1% NP-40, 1mM EDTA, 1mM PMSF, 1x Proteinase inhibitor cocktail (Millipore Sigma)). Extracts from Hi-MYC mouse tumors were prepared in RIPA lysis buffer (0.5% sodium deoxycholate, 0.1% SDS, 20mM Tris-HCl pH7.5, 150mM NaCl, 1% NP-40, 1mM EDTA, 1mM PMSF, 1x Protease inhibitor cocktail (Sigma). Protein concentration was

determined using bicinchoninic acid reagent (Pierce, ThermoFisher Scientific). Immunoblotting was performed essentially as described previously (13), with the following modifications. Twenty-five to 40 µg of protein extract were separated on 7.5% SDS-PAGE. Primary antibodies and working dilutions were: anti-AR (Santa Cruz, cat. no. SC-816, 1:500); anti-GR (Cell Signaling, clone D8H2, 1:1000) and anti-GAPDH (Cell Signaling, cat. No. 2118, 1:2000). Specific protein signal was captured using a cooled charge-coupled digital camera system (Kodak 4000R), quantitated using Kodak Molecular Imaging software and normalized using GAPDH levels, as indicated.

Single cell RNA-sequencing and data analysis

Mouse prostate tumor tissue was dissociated for single cell RNA sequencing using the Tumor Dissociation kit from Miltenyi Biotec (cat. no. 130-096-730). Briefly, tissue was excised, washed with chilled 1x PBS, placed in a petri dish on ice, cut into 2-4 mm^3 pieces, transferred to a gentleMACS C tube containing DMEM/enzyme mix and then attached to gentleMACS Octo Dissociator with heating running the '37C_m_TDK_1' program. The suspension was filtered through a 40 µm cell strainer (Falcon). The cells were harvested by centrifugation at 400g for 10 min and resuspended in chilled 1X Red Blood Cell Removal Solution (Miltenyi Biotec, cat. no.130-094-183). Debris was then removed using the Debris Removal Solution (Miltenyi Biotec, cat. no. 130-109-398) following the manufacturer's instructions.

Single cell gene expression libraries were generated using the 10X Genomics Chromium platform and sequenced on a NovaSeq 6000 (Illumina). Count data from all cells (n = 26,011) were included in a 'SingleCellExperiment' (version 1.8.0) object (14). Quality control, analysis and visualization of scRNAseq data were performed in R (version 3.6.0). Transcripts from a given cell were removed from the analysis if the corresponding transcriptome met any of the following criteria: 20% or more reads aligned to mitochondrial genes, 1500 total counts per cell or less, or 600 genes per cell or less. This yielded a total of 18,166 cells for analysis. The 'scater' package (version 1.14.5) was used to normalize counts per million (CPM) (15). The

dimensionality of this transcriptomic data was reduced using the t-distributed stochastic neighbor embedding (t-SNE) algorithm (16). The 'limma' package (17) was used to identify differentially expressed genes to refine the assignment of clusters generated by the t-SNE algorithm. Briefly, clusters with high-level expression of EPCAM, KRT8, KRT18 and KRT19 were identified as epithelial cells; B cell populations were determined by CD79A, CD79B, CD19; NK and T cells by NKG7, KLRD1, CD3D, CD3E and CD3G; myeloid I by H2 genes and Cd74; myeloid II by S100A8/A9 and cytokines including CCL3, CCL4; non-immune stromal cells by COL3A1, COL1A2, and CD34; and seminal vesicle epithelial (SV) cells by SVS2, SVS5 and KRT18. Only cells with non-zero counts of NR3C1 (GR) were used to compare GR mRNA expression. To determine if glucocorticoid-related gene transcription was induced post-castration, we conducted gene set enrichment analysis (GSEA) (18) for 'all cells' (seminal vesicle excluded) and 'epithelial (tumor) cells', respectively. Low variance, low expression genes of all cells and epithelial cells were removed before performing GSEA. GSEA software (version 4.1.0) was used with classic enrichment, inclusion gene set size between 15 and 500, and the number of permutations set to 1000. A P-value cutoff of 0.05 with a false discovery rate (FDR q-val) cutoff of 0.25 were considered statistically significant.

RESULTS

Ultrasound imaging to monitor changes in prostate tumor volume in GEMMs.

We have previously established the precision and reproducibility of magnetic resonance (MR) (19) and high frequency ultra-sound (HFUS) (6) imaging protocols for monitoring the volume of normal prostate as well as prostate cancers (13) in murine models. We compared the utility of HFUS and MR imaging by sequentially imaging three mice bearing MYC driven prostate cancers with both modalities. Both HFUS and MR imaging showed a high degree of correlation for tumor volume determination (Supplementary Fig. 1). MR imaging has a higher resolution, and it is therefore easier to visually distinguish tumor boundaries, but image capture itself is slower and

more expensive. For HFUS imaging, image capture is faster and the three-dimensional nature of the HFUS data in combination with AMIRA software allows semi-automated segmentation to determine tumor volume (6). Therefore, we employed the HFUS methodology in these studies to maximize data acquisition (number of mice and number of volume determinations per mouse).

Castration induces delayed regression in a PTEN-deficient mouse model.

To determine the effects of castration on primary prostate cancers, we surgically castrated groups of mice bearing PTEN-deficient prostate cancers, and serially imaged each mouse using HFUS to determine the change in tumor volume over time. In the male mice of this GEMM, loss of PTEN expression occurs - at puberty - in the prostate epithelial cells and leads to the development of PTEN-deficient prostate cancers, with essentially 100% penetrance. Fig. 1 demonstrates that, following castration, PTEN-deficient tumors continue to increase in volume for seven days, before beginning to regress. During the initial 7 days post-castration, the average volume of the tumors in the castrated mice were indistinguishable from sham-operated mice (Fig. 1B), suggesting that the prostate tumors were growing at the same rate in castrated and intact hosts. We tracked the tumor volume in multiple cohorts of the same GEMM, that differed in average initial tumor volume (Fig. 2A-D). Almost all showed a delay in the onset of regression, and the length of the delay correlated with the initial volume of the tumor (Fig. 2E).

To determine if the increase in tumor volume in castrated mice is due to an inflammatory infiltrate or accompanying edema, we castrated mice, sacrificed these animals at 6 and 14 days post-castration, fixed the tumors and examined H&E stained tissue sections. Sham operated animals provided controls. Pathological examination of the histological tissue sections revealed no significant inflammatory infiltration within the glands or within the surrounding stroma (Fig. 3A). Tissue sections from the same set of mice were immunohistochemically stained for Ki67 expression (Fig. 3B), to determine the rate of proliferation of the epithelial tumor cells within the prostate. When we ranked tumors by a Ki67 index (Fig. 3C), we observed that three (of the four) mice sacrificed at 6d post-castration were among the animals with the highest Ki67 indices. This

suggests that there was a transient increase in the proliferation of the prostate tumor cells during the six days following castration which contributes to the volume increase that defines the delayed regression phenotype we have observed.

Intra-tumoral androgen production could account for the transient proliferative response to castration that leads to the delay in regression. We therefore measured androgen levels in prostate tumor tissue. Following castration, testosterone and dihydrotestosterone levels decreased to undetectable levels and remained undetectable for at least two weeks (Fig. 4A-B). Other androgen precursors were not induced following castration (Supplementary Fig. 2B-D).

Castration-induced regression delay is mediated by GR signaling.

Since it appears that androgen-dependent signaling is not responsible for the regression delay we have observed, we hypothesized that glucocorticoid-GR signaling could partially compensate for the loss of AR signaling and mediate the regression delay. To test our hypothesis, we measured intra-tumoral endogenous ligands of GR. Two glucocorticoids that are active GR ligands (20) – corticosterone and deoxycorticosterone – showed a modest increase post-castration (Fig. 5A). Interestingly, the levels of two precursors (5a-dihydroprogesterone and pregnenolone; Fig. 5B) were reduced, suggesting that sustained levels of corticosterone and deoxycorticosterone might be caused in large part by the generation of corticosterone from inactive 11-dehydrocorticosterone (Fig. 5B) by 11ß-HSD1, in the absence of 11ß-HSD2 (21). ADT may also upregulate hexose-6-phosphate dehydrogenase, which generates NADPH required for 11ß-HSD1 activity (22). Since the levels of glucocorticoid ligands were sustained, we sought to determine if GR signaling was necessary for the observed delay in regression, by blocking GR ligand binding using the antagonist CORT125281. CORT125281 is one of a series of novel glucocorticoid receptor modulators (23, 24) that are more selective than older antagonists such as RU486 (8). Fig. 5B shows that treatment with CORT125281 (GRi) reduced the regression delay in PTEN-deficient tumors. Next, we examined these phenomena in a second murine model of primary prostate cancer (the Hi-MYC GEMM), driven by prostate epithelial cell-specific over-

expression of c-MYC (10). We observed that castration of these mice was also followed by a delay in regression (Fig. 6A) with a remarkably similar kinetic profile to the PTEN-deficient model (compare Figs. 1B and 6A), although the delay appears to be closer to 3 days than 7 days. Importantly, administration of CORT125281 was also effective in reducing the delay in the onset of castration-induced regression in the Hi-MYC GEMM (Fig. 6B).

GR expression and signaling is increased during the period of delayed regression

Since castration-induced enhanced GR signaling is required at least in part for the delayed regression phenotype (Fig. 5A), we measured changes in the level of GR protein and mRNA expression in tumor tissue, at the end of the delay period and compared those expression levels to the non-castrated tumor-bearing mice. Immunoblot analysis of prostate tumor lysates from both the PTEN-loss and MYC-gain GEMMs showed that near the end of the delay period (i.e., 3-4 days post-castration) the relative level of GR protein was elevated in both models (Fig. 7).

Next, we employed single cell RNA sequencing (scRNAseq) to assess changes in the GR mRNA, in the tumor cell population. Specifically, mice bearing PTEN-deficient tumors were either castrated (n=2) or sham operated (n=2), and sacrificed near the end of the delay period. Tumors were dissociated into single cells and these were subjected to RNA sequencing. Transcript counts from single cells of tumors from all four mice were pooled and the dimensionality of this transcriptomic data was reduced using the t-distributed stochastic neighbor embedding (t-SNE) algorithm. t-SNE visualization of the compiled transcript dataset, followed by hierarchical clustering and subjective cell annotation based on transcript function, allowed us to identify seven relevant cell types within the tumor population (Fig. 8A). In Fig. 8B, we projected CD45 (hematopoietic/immune cell lineage) and EPCAM (epithelial cell lineage) expression on to the t-SNE plot from Fig. 8A. This confirms the expected lineage of the putative cell population assignments. We then repeated the t-SNE analysis and hierarchical clustering for each of the four individual samples and determined the number of GR transcripts in both the entire GR transcript-positive cell population (all GR+ cells) and in the GR+ epithelial cell population, as

shown in Supplementary Fig. 5 (upper panels). Pooling of like samples revealed that GR transcript levels are increased – four days post-castration, relative to sham-operated mice – in the epithelial cell population of the tumor (Fig. 8C), but not in the entire tumor cell population, which included stromal and immune cell populations, but not seminal vesicle (Supplementary Fig. 5, lower panels).

Focusing on only those transcripts expressed by the epithelial cell cluster, we performed a differential gene expression analysis comparing the pooled transcript data from the prostate cancers of the sham-operated mice with those from the four-day post-castration mice. Gene-set enrichment analysis (GSEA) (18) of differentially expressed genes demonstrated that a glucocorticoid signaling gene set (PID_REG_GR_PATHWAY) was significantly upregulated in the epithelial cell population (Fig. 8D and Supplementary Fig. 6B). Importantly, in addition to the GR (N3RC1) itself, ~50% (16/31) of the enriched genes are related to cell cycle, apoptosis, mitogenesis or tumorigenesis (Supplementary Table 1). In contrast, GSEA of the total tumor cell population – as in Fig. 8C – demonstrated that a separate glucocorticoid signaling pathway (WR_GLUCOCORTICOID_RECEPTOR_PATHWAY) was significantly upregulated (Supplementary Fig. 6A). Only ~20% (3/14) of the enriched genes (plus GR/N3RC1) in this pathway are related to cell cycle, apoptosis, mitogenesis or tumorigenesis (Supplementary Table 2).

DISCUSSION

We used HFUS imaging to determine the kinetics of tumor volume following castration in two murine models of prostate cancer driven by genetic alterations (PTEN loss, MYC over-expression) that are common in human prostate cancer. Surprisingly, we found that in the 4-7 day period immediately following castration-induced androgen deprivation, the prostate cancer tumor volumes in both models continued to increase, at a rate that was indistinguishable from tumors in untreated mice (Figs. 1 and 6). We monitored the kinetics of tumor volume following

castration in mice grouped according to initial (pre-castration) tumor volume and found that the regression delay was proportional to the initial tumor volume (Fig. 2). During the regression delay there is an increase in tumor volume of 10-20%, yet there is no discernable inflammatory or immune cell infiltrate in H&E tissue sections taken from tumors harvested just prior to the beginning of tumor regression (Fig. 3A). Moreover, there is an increase in expression of the proliferative marker Ki67, detectable in the epithelial tumor cell population by the end of the delay period (Fig. 3B-C). Taken together, these data suggest that the unexpected increase in tumor volume following castration is due to continued proliferation of the epithelial tumor cell population, even as castration triggers the apoptotic process that ultimately leads to regression of the prostate cancer.

The studies of Huggins (25) in the 1940's first demonstrated that prostate cancer growth is dependent on testicular androgens. In the 80 years since, it has become clear that proliferation is dependent on signaling through the androgen receptor. In prostate cancer, a variety of initiating mutations in FoxA1, HoxB13, SPOP and other genes converge on a common mechanism – reprogramming of the AR cistrome – inducing the transcription of a set of genes that drive tumor cell proliferation in response to androgens (3, 26, 27). Since we did not detect any residual androgens in tumor extracts from the PTEN-deficient mice (Fig. 4), we assumed that conventional signaling through the AR has been turned off. Therefore, we sought to determine whether signaling through the GR, a member of the nuclear receptor super-family that is closely related to the AR, substitutes for AR signaling following castration and during the subsequent delayed regression period. Indeed, our key finding is that CORT125281, a highly selective glucocorticoid receptor blocker (23, 24), reduced the regression delay in both the PTEN-deficient (Fig. 5D) and the Hi-MYC (Fig. 6B) prostate cancer models. This strongly supports a role for GR-signaling in the delay period that follows castration.

We examined the PTEN-deficient model in detail at the molecular level and, consistent with the requirement for GR signaling, we observed an increase in key components of the

signaling pathway: glucocorticoid ligands (Fig. 5A) as well as the glucocorticoid receptor (both protein and mRNA; Figs. 7A and 8C, respectively). We used single cell transcriptomic analysis to determine the changes in the level of GR mRNA in the tumor cell population only, since GR is widely expressed and serves different functions in different cell populations within the tumor and its associated microenvironment. Indeed, when we combined the scRNAseq data from all of the cell populations we identified in Fig. 8A, we did not observe a difference in the number of GR transcripts per cell (Supplementary Fig. 5). When we performed bulk RNAseq analysis on similar tumors, we also saw no difference in GR transcripts/cell at the same time points post-castration (data not shown) further confirming the utility and resolving power of the single cell methodology. Another important observation from our transcriptomic analysis concerns the GR-regulated gene sets identified by GSEA. When we analyzed the epithelial cell population only, we found a gene set that had a larger fraction of genes which we subjectively identified as having a tumorigenic or proliferative function, relative to the GR gene set identified by GSEA of all of the cell populations depicted in the t-SNE plot (Supplementary Tables 1-2). Finally, although we did not perform a complete set of molecular analyses on the Hi-MYC model, we observed that GR protein was also elevated in tumors post-castration (Fig. 7B), similar to our observations in the PTEN-deficient GEMM (Fig. 7A). This suggests a similar mechanism is operative in two genetically distinct models.

The immediate, transient response to androgen that we have documented – an increase in GR signaling that is a consequence of both increased levels of active glucocorticoids and increased expression of the GR – is very similar to the response to AR signaling blockade that has been observed in a subset of castration resistant prostate cancers. Specifically, Arora *et al.* (28) and others (29, 30) have shown that GR substitutes for the AR to overcome enzalutamide resistance in murine models of prostate cancer and that the mechanism involves increased GR expression. Similar studies from Xie *et al.* (31) strongly support our observations. First, they describe a transcriptional model where AR signaling negatively regulates GR/N3RC1

transcription. This mechanism may well be operative in our GEMMs, although it does not account for the transient nature of the regression delay that we have documented. Second, in a model of ADT that employs AR gene silencing, there is a clear pattern of delayed regression that is very similar to the pattern we observe in Figs. 1, 2 and 6A, although these authors do not comment on this aspect of their data (31). Finally, they demonstrate that GR expression is induced in samples of human prostate cancer, when patients are given neo-adjuvant hormonal therapy (31).

Sharifi and colleagues (21, 22) have documented that sustained levels of glucocorticoids is another mechanism that can contribute to GR 'takeover' in enzalutamide resistant prostate cancers. In human cells, they have identified mechanisms that are driven by androgen suppression and lead to the production of cortisol from the inactive metabolite cortisone, by degrading 11ß-HSD2 (21) or enhancing the reductive activity of 11ß-HSD1 via increased H6PD expression (22). An analogous set of mechanisms could generate active corticosterone from inactive 11-dehydrocorticosterone (Fig. 5B) in our models, following castration.

Finally, our observation of sustained proliferation in the context of androgen deprivation, driven by GR signaling has potential implications for prostate cancer therapy, as others have noted (28, 30, 32). Specifically, our data support the idea of combining AR and GR blockade and also reducing the use of glucocorticoids in combination with other therapies for castration resistant prostate cancers.

ACKNOWLEDGEMENTS

We thank Corcept Therapeutics for providing CORT125281.

FIGURE LEGENDS

Figure 1. Castration induces delayed regression of PTEN-deficient prostate cancers. Tumor-bearing PB-Cre4:Pten$^{fl/fl}$ mice were sham-operated (None) or castrated (CX) and the

mouse tumors serially imaged by HFUS at the indicated times post-surgery. A. Three-dimensional prostate tumor reconstructions. HFUS images from the castrated mice (P364, P377, P380 and P386) were segmented in three dimensions with AMIRA software and the tumor pseudo-colored green. Tumors arise in both anterior lobes and HFUS images were captured separately for the right (R) and left (L) lobes. **B.** Kinetics of tumor volume following castration. Tumor volumes were determined from the 3D reconstructions, at the indicated times post-castration (n=4, blue) or post-sham operation (n=3, red) and plotted as percent pre-castration volume (mean [%] ± SEM).

Figure 2. Regression delay is dependent on pre-castration tumor volume. Tumor-bearing PB-Cre4:Pten$^{fl/fl}$ mice were castrated, tumors were serially imaged and volumes were determined using HFUS, followed by segmentation with AMIRA software, as described in Fig. 1. **A-D.** Kinetics of tumor volume following castration. Mean tumor volume for groups of mice (n = 4-6) corresponding to pre-castration tumor volumes of: ~250 mm^3 (**A**); Two groups ~500 mm^3 (**B**); Two groups ~700 mm^3 (**C**) and ~1000 mm^3 (black line) or ~1700 mm^3 (grey line) (**D**). For each panel. tumor volumes were determined from 3D reconstructions, at the indicated times post-castration and plotted as tumor volume (mean volume [mm^3] ± SEM). **E.** Regression delay increases with pre-castration tumor volume. Data derived from the groups shown in **A-D**.

Figure 3. Castration does not induce an inflammatory cell infiltrate, but transiently increases tumor cell proliferation. Tumor-bearing PB-Cre4:Pten$^{fl/fl}$ mice were sham-operated (Sham) or castrated (CX), sacrificed 6 or 14 days post-surgery and tumors were then excised, fixed and sectioned. **A.** H&E staining of paraffin-embedded tumor tissue sections, 200x magnification. **B.** Immunohistochemical staining (brown) for Ki67, 400x magnification**. C.** Ranked-

order box plot of Ki67 index for the indicated sets of tumors (n=4). The Ki67 index was determined as described in the **Materials and Methods**. The data were log transformed, plotted in rank-order and analyzed using a linear mixed model (F=20.05,2,70).

Figure 4. Castration reduces intra-prostatic testosterone and dihydrotestosterone to undetectable levels. Tumor-bearing PB-Cre4:Pten$^{fl/fl}$ mice (n=4 for each time point) were castrated, sacrificed and tumor tissue excised. Androgen levels were determined using LC/MS/MS, as described in the **Materials and Methods**. **A-B.** Tumor testosterone (**A**) and dihydrotestosterone (**B**) levels for individual mice, at the indicated times post-castration.

Figure 5. Inhibition of enhanced glucocorticoid signaling blocks castration-induced delayed regression in PTEN-deficient prostate cancers. A. Tumor glucocorticoid levels. Tumor-bearing PB-Cre4:Pten$^{fl/fl}$ mice were castrated, sacrificed and tumor tissue excised. Levels of the indicated glucocorticoids were determined using LC/MS/MS, as described in the **Materials and Methods**. **B.** Scheme illustrating glucocorticoid steroid metabolism. Levels for steroids in bold type are shown in panel **A**. The arrows are not meant to reflect chemical equilibria but rather net synthesis. Steroid abbreviations (trivial name): Chol (cholesterol); Preg (pregnenolone); Prog (progesterone); DHP (5a-dihydroprogesterone); DOC (11-deoxycorti-costerone); Cort (corticosterone); DHC (11-dehydrocorticosterone). **C.** Tumor-bearing PB-Cre4:Pten$^{fl/fl}$ mice were castrated and treated with CORT125281 (CX+GRi). Tumors were serially imaged and volumes determined as in Fig. 1. Three-dimensional prostate tumor reconstructions from representative mice treated with CORT125281 (P443, P429) are shown. **D.** Kinetics of tumor volume following castration, in the presence of a GR inhibitor. Tumor volumes were determined from the 3D reconstructions, at the indicated times post-castration in mice receiving CORT125281 (n=6,

orange) and plotted as percent pre-castration volume (mean [%] ± SEM). Tumor volumes from mice which were castrated and not treated are re-plotted from Fig. 1 (n=4, blue).

Figure 6. Castration-induced delayed regression of Hi-MYC prostate cancers is also dependent on glucocorticoid signaling. Tumor-bearing ARR_2/PB-*Myc* mice were sham-operated (None), castrated (CX) or castrated and treated with CORT125281 (CX+GRi). Tumors were serially imaged and volumes determined as in Fig. 1. **A.** Upper panel: Three-dimensional prostate tumor reconstructions from representative castrated Hi-MYC mice (P414, P406). Lower panel: Kinetics of tumor volume following castration. Tumor volumes were determined from the 3D reconstructions, at the indicated times post-surgery in castrated (n=7, blue) or sham-operated (n=7, red) mice and plotted as percent pre-castration volume (mean [%] ± SEM). **B.** Upper panel: Three-dimensional prostate tumor reconstructions from representative Hi-MYC mice which were castrated and received CORT125281 (P457, P460). Lower panel: Kinetics of tumor volume following castration. Tumor volumes were determined from the 3D reconstructions, at the indicated times post-castration in mice receiving CORT125281 (n=5, orange) or mice which were only castrated and received no drug (n=6, blue). These values were plotted as percent pre-castration volume (mean [%] ± SEM).

Figure 7. GR protein levels increase four days following castration. Groups (n=4) of tumor-bearing mice were sham-operated (SH) or castrated (CX). Three or four days later (as indicated), mice were sacrificed, tumor tissue excised, protein lysates were prepared, immunoblot analyses of AR and GR proteins were performed in triplicate and protein levels were quantitated, as described in the **Materials and Methods**. **A.** PTEN-deficient GEMM. Representative immunoblots from tumors that developed in PB-Cre4 *P* $Pten^{fl/fl}$ mice (upper panels) are shown.

Relative levels of AR and GR protein, normalized to GAPDH, were derived from triplicate immunoblots (lower panels). **B.** Hi-MYC GEMM. Representative immunoblots from tumors that developed in ARR_2/PB-*Myc* mice (upper panels) are shown. Relative levels of AR and GR protein, normalized to GAPDH, were derived from triplicate immunoblots (lower panels). Corresponding complete immunoblot images for both **A** and **B** are shown in Supplemental Fig. 4.

Figure 8. Single cell transcriptome analysis demonstrates that GR mRNA and GR-regulated genes are increased during the regression delay. Tumor-bearing PB-Cre4:Pten$^{fl/fl}$ mice were castrated (n=2) or sham operated (n=2), sacrificed four days later and tumor tissue excised. The tumor was dissociated into single cells and for each sample RNA from about 5,000 cells was sequenced, as described in the **Materials and Methods**. **A.** t-Distributed stochastic neighborhood embedding (t-SNE) visualization of single cell mRNA data from all four mice, followed by hierarchical clustering and gene transcript annotation. Seven cell sub-populations were identified and color-coded as indicated by the labels in the panel: epithelial (tumor epithelial cells); NK+T (NK cells, T-cells); myeloid I and II (two distinct myeloid cell populations); stromal (fibroblast, myofibroblast and endothelial cells); B-cells; and SV (seminal vesicle). **B.** Relative expression of CD45 (red) and EPCAM (blue) mRNAs in the cell clusters identified in panel A. Darker color indicates higher level of mRNA expression (transcript counts). The stromal cluster is shaded black to indicate that it does not have significant expression of either mRNA. **C.** GR mRNA expression is increased four days post-castration (CX-D4) relative to sham-operated mice (SH-D4). Box plot of transcript counts corresponding to GR-expressing epithelial cells identified in panel **A**. (28)ta from individual mice is shown in Supplementary Fig. 5 (right side). **D.** GSEA demonstrates increased GR signaling during the regression delay. Differential gene expression of the pooled transcripts from the epithelial cell population followed by GSEA identified one glucocorticoid signaling gene set (PID_REG_GR_PATHWAY) that was significantly upregulated

in the epithelial cell population.

FIGURE 1

A

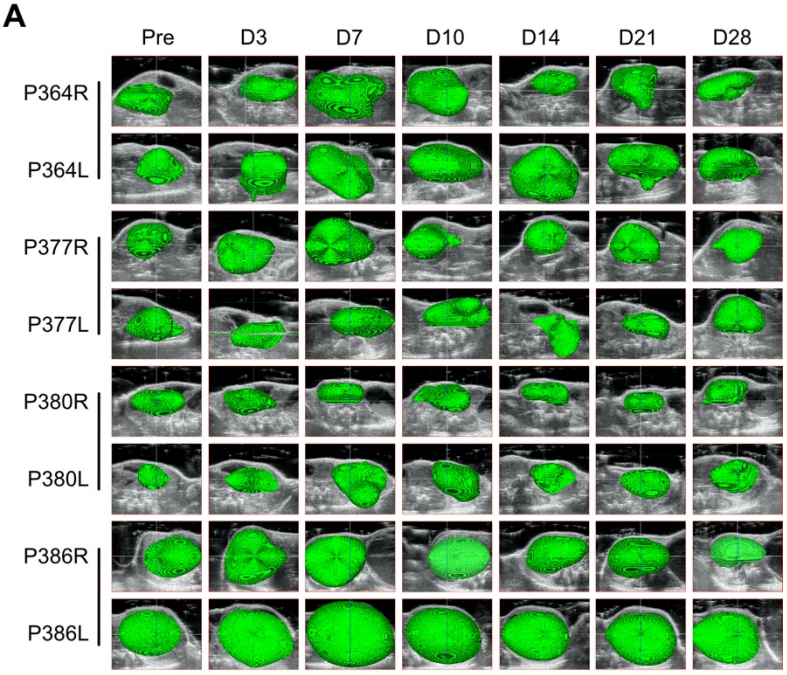

B

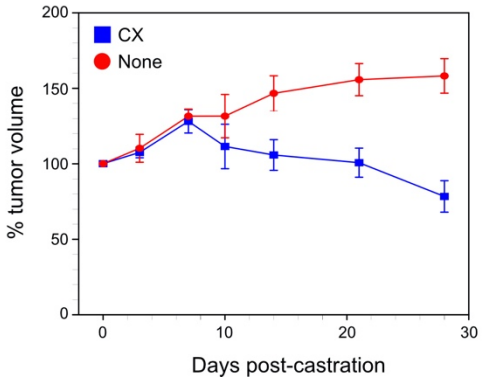

FIGURE 2

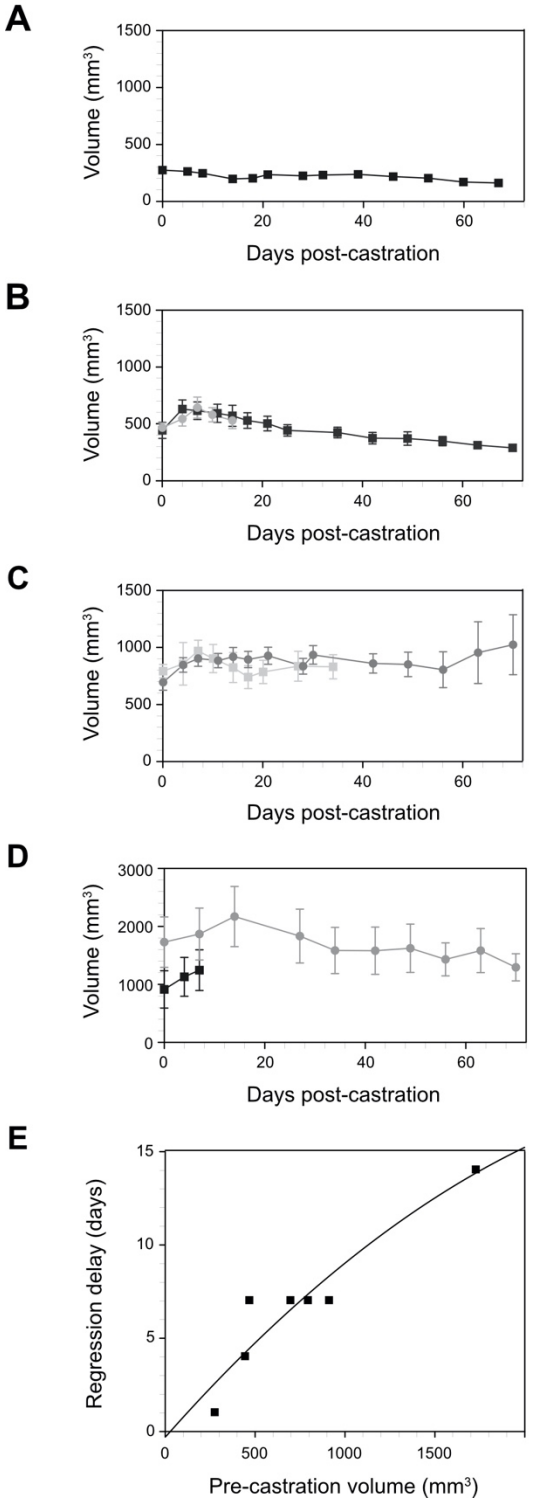
A
Volume (mm³)
1500
1000
500
0
0
20
40
60
Days post-castration
B
Volume (mm³)
1500
1000
500
0
0
20
40
60
Days post-castration
C
Volume (mm³)
1500
1000
500
0
0
20
40
60
Days post-castration
D
Volume (mm³)
3000
2000
1000
0
0
20
40
60
Days post-castration
E
Regression delay (days)
15
10
5
0
0
500
1000
1500
Pre-castration volume (mm³)

FIGURE 3

A H&E:

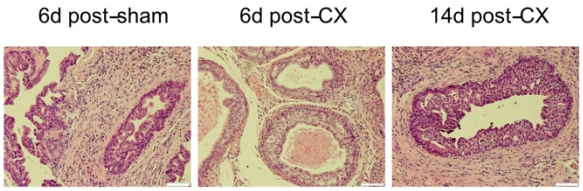

B Ki67:

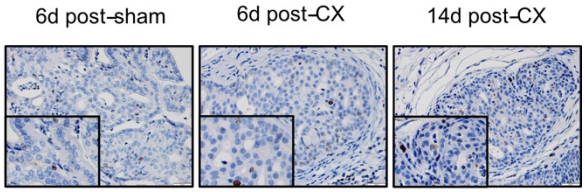

C

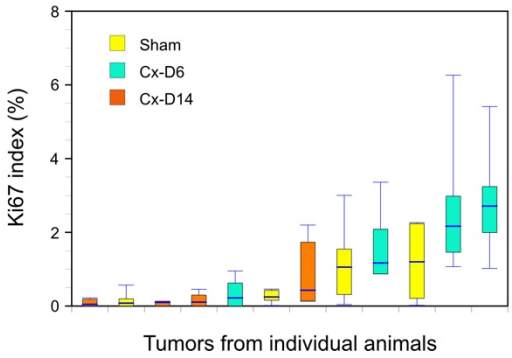

FIGURE 4

A

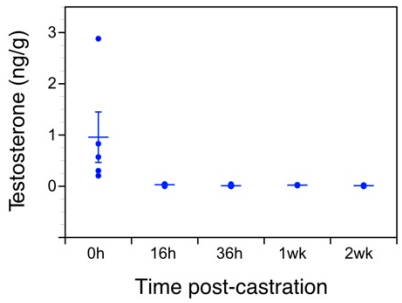
Testosterone (ng/g)
3
2
1
0
0h
16h
36h
1wk
2wk
Time post-castration

B

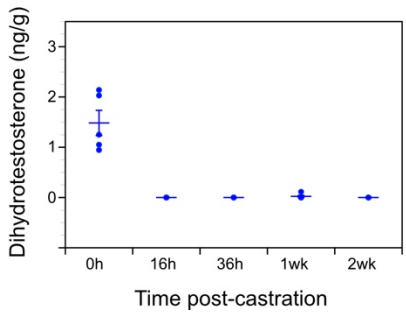
Dihydrotestosterone (ng/g)
3
2
1
0
0h
16h
36h
1wk
2wk
Time post-castration

FIGURE 5

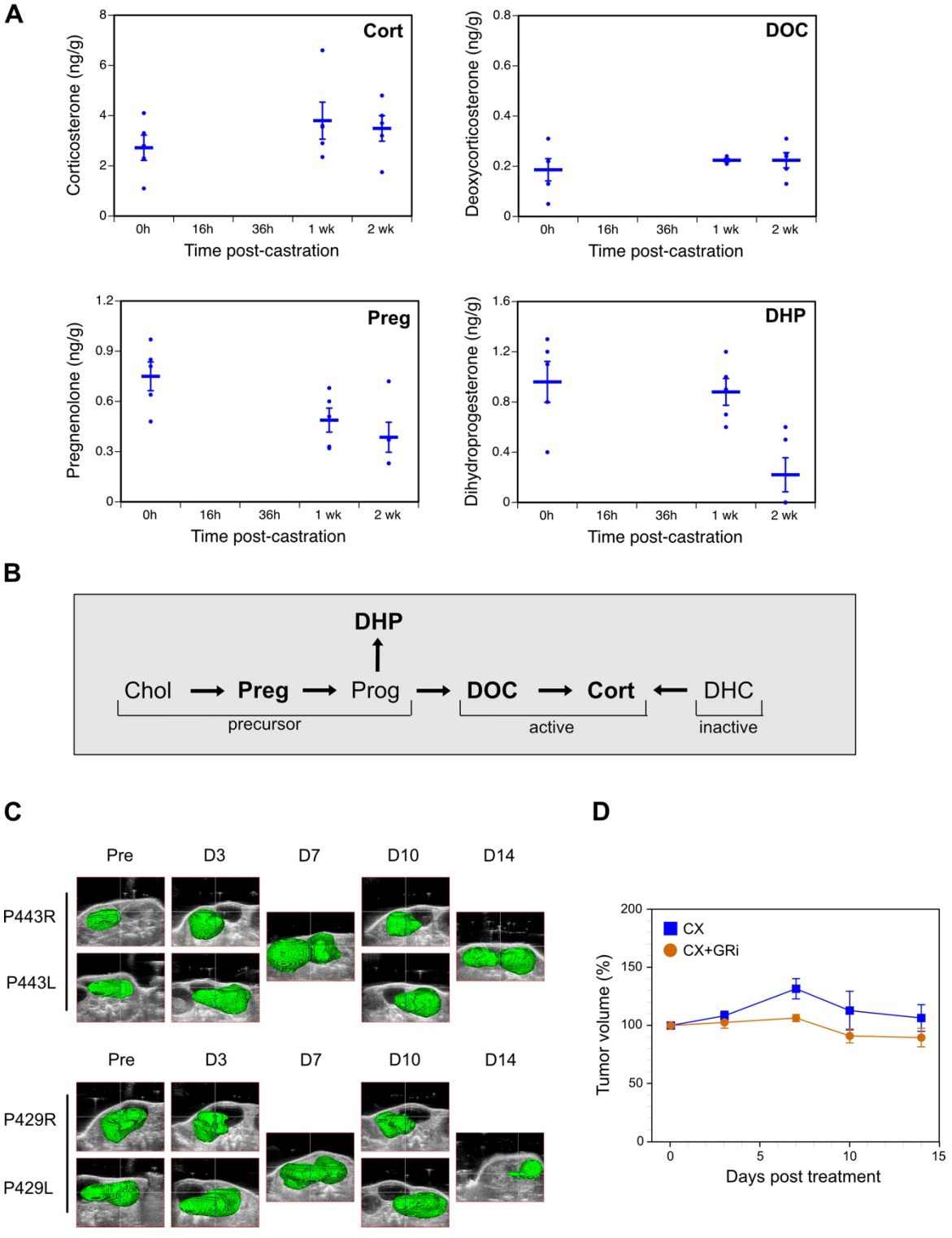
A
Cort
Corticosterone (ng/g)
DOC
Deoxycorticosterone (ng/g)
Preg
Pregnenolone (ng/g)
DHP
Dihydroprogesterone (ng/g)
0h
16h
36h
1 wk
2 wk
Time post-castration
B
DHP
Chol
Preg
Prog
DOC
Cort
DHC
precursor
active
inactive
C
Pre
D3
D7
D10
D14
P443R
P443L
P429R
P429L
D
CX
CX+GRi
Tumor volume (%)
Days post treatment

FIGURE 6

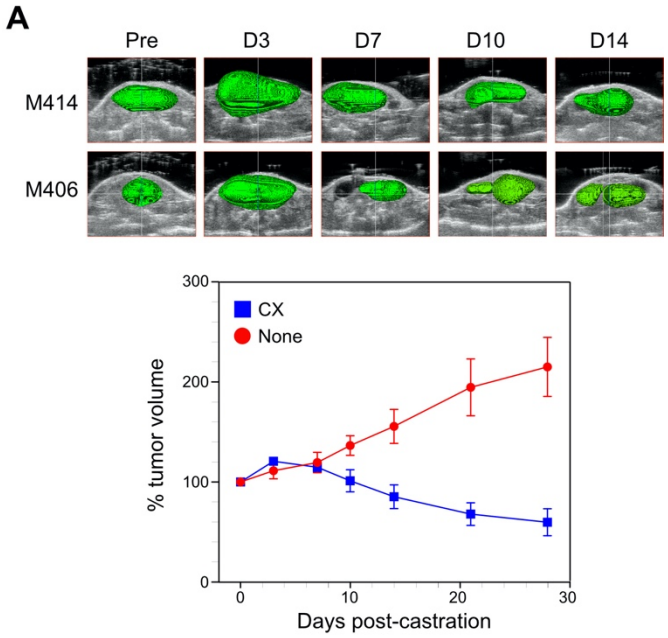
A
Pre
D3
D7
D10
D14
M414
M406
CX
None
% tumor volume
Days post-castration
0
100
200
300
0
10
20
30

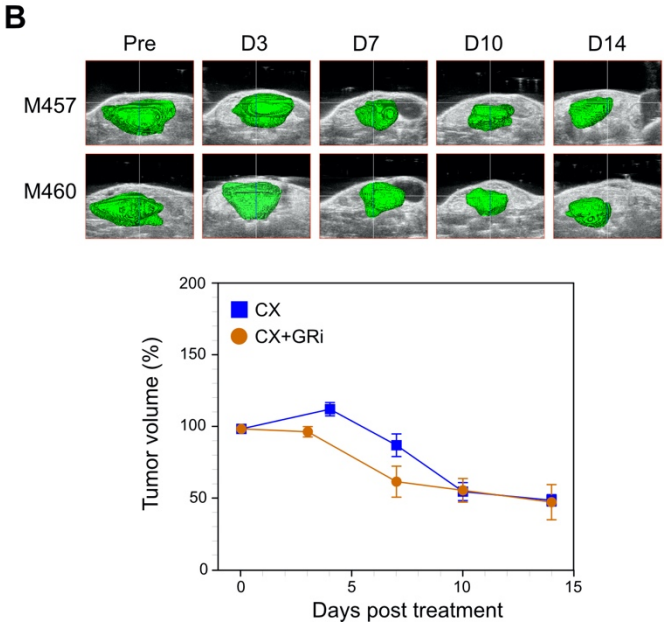
B
Pre
D3
D7
D10
D14
M457
M460
CX
CX+GRi
Tumor volume (%)
Days post treatment
0
50
100
150
200
0
5
10
15

FIGURE 7

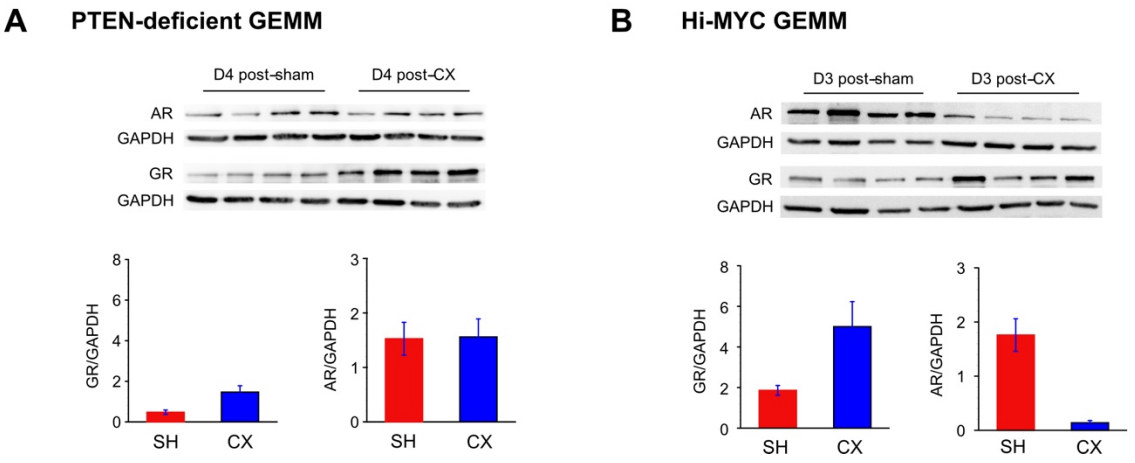

FIGURE 8

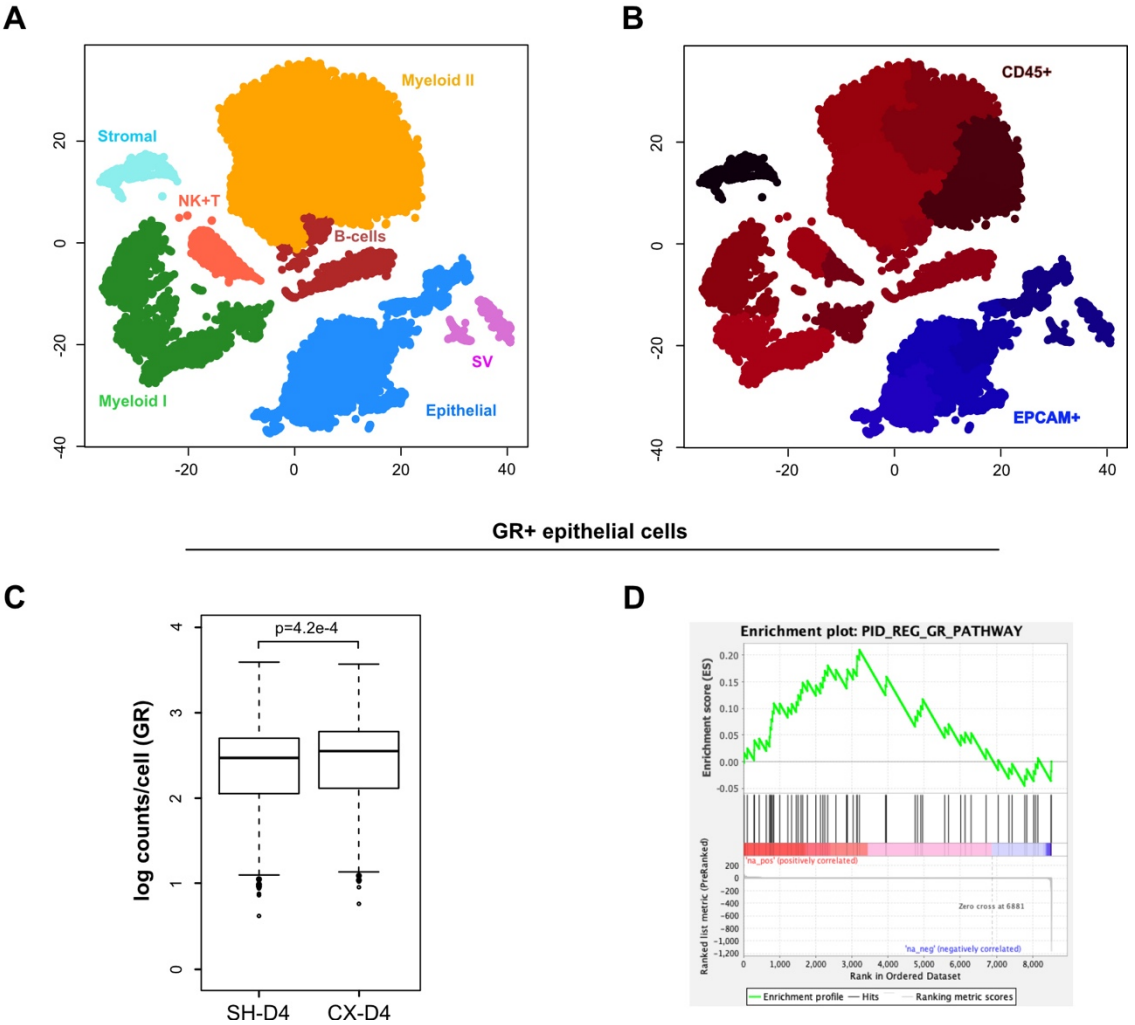

References

1. Siegel RL, Miller KD, Jemal A. Cancer statistics, 2020. CA Cancer J Clin 2020;70:7-30.

2. Teo MY, Rathkopf DE, Kantoff P. Treatment of Advanced Prostate Cancer. Annu Rev Med 2019;70:479-99.

3. Pomerantz MM, Li F, Takeda DY, Lenci R, Chonkar A, Chabot M*, et al.* The androgen receptor cistrome is extensively reprogrammed in human prostate tumorigenesis. Nat Genet 2015;47:1346-51.

4. Sartor O, de Bono JS. Metastatic Prostate Cancer. N Engl J Med 2018;378:645-57.

5. Arriaga JM, Abate-Shen C. Genetically Engineered Mouse Models of Prostate Cancer in the Postgenomic Era. Cold Spring Harb Perspect Med 2019;9

6. Singh S, Pan C, Wood R, Yeh CR, Yeh S, Sha K*, et al.* Quantitative volumetric imaging of normal, neoplastic and hyperplastic mouse prostate using ultrasound. BMC Urol 2015;15:97.

7. Davis JS, Nastiuk KL, Krolewski JJ. TNF is necessary for castration-induced prostate regression, whereas TRAIL and FasL are dispensable. Mol Endocrinol 2011;25:611-20.

8. Kach J, Long TM, Selman P, Tonsing-Carter EY, Bacalao MA, Lastra RR*, et al.* Selective Glucocorticoid Receptor Modulators (SGRMs) Delay Castrate-Resistant Prostate Cancer Growth. Mol Cancer Ther 2017;16:1680-92.

9. Wang S, Gao J, Lei Q, Rozengurt N, Pritchard C, Jiao J*, et al.* Prostate-specific deletion of the murine Pten tumor suppressor gene leads to metastatic prostate cancer. Cancer Cell 2003;4:209-21.

10. Ellwood-Yen K, Graeber TG, Wongvipat J, Iruela-Arispe ML, Zhang J, Matusik R*, et al.* Myc-driven murine prostate cancer shares molecular features with human prostate tumors. Cancer Cell 2003;4:223-38.

11. Koorneef LL, Kroon J, Viho EMG, Wahl LF, Heckmans KML, van Dorst M*, et al.* The selective glucocorticoid receptor antagonist CORT125281 has tissue-specific activity. J Endocrinol 2020;246:79-92.

12. Wilton JH, Titus MA, Efstathiou E, Fetterly GJ, Mohler JL. Androgenic biomarker prof|ling in human matrices and cell culture samples using high throughput, electrospray tandem mass spectrometry. Prostate 2014;74:722-31.

13. Pan C, Jaiswal Agrawal N, Zulia Y, Singh S, Sha K, Mohler JL*, et al.* Prostate tumor-derived GDF11 accelerates androgen deprivation therapy-induced sarcopenia. JCI Insight 2020;5

14. Amezquita RA, Lun ATL, Becht E, Carey VJ, Carpp LN, Geistlinger L*, et al.* Orchestrating single-cell analysis with Bioconductor. Nat Methods 2020;17:137-45.

15. McCarthy DJ, Campbell KR, Lun AT, Wills QF. Scater: pre-processing, quality control, normalization and visualization of single-cell RNA-seq data in R. Bioinformatics 2017;33:1179-86.

16. van der Maaten L, Hinton G. Visualizing Data using t-SNE J Mach Learning Res 2008;9:2579-605.

17. Ritchie ME, Phipson B, Wu D, Hu Y, Law CW, Shi W*, et al.* limma powers differential expression analyses for RNA-sequencing and microarray studies. Nucleic Acids Res 2015;43:e47.

18. Subramanian A, Tamayo P, Mootha VK, Mukherjee S, Ebert BL, Gillette MA*, et al.* Gene set enrichment analysis: a knowledge-based approach for interpreting genome-wide expression profiles. Proc Natl Acad Sci U S A 2005;102:15545-50.

19. Nastiuk KL, Liu H, Hamamura M, Muftuler LT, Nalcioglu O, Krolewski JJ. In vivo MRI volumetric measurement of prostate regression and growth in mice. BMC Urol 2007;7:12.

20. Brookes JC, Galigniana MD, Harker AH, Stoneham AM, Vinson GP. System among the corticosteroids: specificity and molecular dynamics. J R Soc Interface 2012;9:43-53.

21. Li J, Alyamani M, Zhang A, Chang KH, Berk M, Li Z*, et al.* Aberrant corticosteroid metabolism in tumor cells enables GR takeover in enzalutamide resistant prostate cancer. eLife 2017;6.

22. Li J, Berk M, Alyamani M, Sabharwal N, Goins C, Alvarado J*, et al.* Hexose-6-phosphate dehydrogenase blockade reverses prostate cancer drug resistance in xenograft models by glucocorticoid inactivation. Sci Transl Med 2021;13.

23. Morgan BP, Swick AG, Hargrove DM, LaFlamme JA, Moynihan MS, Carroll RS*, et al.* Discovery of potent, nonsteroidal, and highly selective glucocorticoid receptor antagonists. J Med Chem 2002;45:2417-24.

24. Hunt HJ, Belanoff JK, Walters I, Gourdet B, Thomas J, Barton N*, et al.* Identification of the Clinical Candidate (R)-(1-(4-Fluorophenyl)-6-((1-methyl-1H-pyrazol-4-yl)sulfonyl)-4,4a,5,6,7,8-hexah ydro-1H-pyrazolo[3,4-g]isoquinolin-4a-yl)(4-(trifluoromethyl)pyridin-2-yl)methano ne (CORT125134): A Selective Glucocorticoid Receptor (GR) Antagonist. J Med Chem 2017;60:3405-21.

25. Huggins C, Hodges CV. Studies on prostatic cancer I. The effect of castration, of estrogen and of androgen injection on serum phosphatases in metastatic carcinoma of the prostate. Cancer Res 1941;1:293-7.

26. Copeland BT, Du J, Pal SK, Jones JO. Factors that influence the androgen receptor cistrome in benign and malignant prostate cells. Molecular oncology 2019;13:2616-32.

27. Grbesa I, Augello MA, Liu D, McNally DR, Gaffney CD, Huang D*, et al.* Reshaping of the androgen-driven chromatin landscape in normal prostate cells by early cancer drivers and effect on therapeutic sensitivity. Cell Rep 2021;36:109625.

28. Arora VK, Schenkein E, Murali R, Subudhi SK, Wongvipat J, Balbas MD*, et al.* Glucocorticoid receptor confers resistance to antiandrogens by bypassing androgen receptor blockade. Cell 2013;155:1309-22.

29. Puhr M, Hoefer J, Eigentler A, Ploner C, Handle F, Schaefer G*, et al.* The Glucocorticoid Receptor Is a Key Player for Prostate Cancer Cell Survival and a Target for Improved Antiandrogen Therapy. Clin Cancer Res 2018;24:927-38.

30. Isikbay M, Otto K, Kregel S, Kach J, Cai Y, Vander Griend DJ*, et al.* Glucocorticoid receptor activity contributes to resistance to androgen-targeted therapy in prostate cancer. Horm Cancer 2014;5:72-89.

31. Xie N, Cheng H, Lin D, Liu L, Yang O, Jia L*, et al.* The expression of glucocorticoid receptor is negatively regulated by active androgen receptor signaling in prostate tumors. Int J Cancer 2015;136:E27-38.

32. Valle S, Sharifi N. Targeting Glucocorticoid Metabolism in Prostate Cancer. Endocrinol 2021;162.

33. Sharifi N. Minireview: Androgen metabolism in castration-resistant prostate cancer. Mol Endocrinol 2013;27:708-14.

SUPPLEMENTARY TABLES

Supplementary Table 1: Genes from PID_REG_GR_PATHWAY enriched in tumor epithelial cells

SYMBOL	RANK IN GENE LIST	RANK METRIC SCORE	RUNNING ES	CORE ENRICHMENT
STAT1	20	46.70607376	0.016506929	Yes
CDKN1A	108	19.34492683	0.025104519	Yes
EGR1	297	10.04787254	0.021779079	Yes
IRF1	303	9.985536575	0.040056754	Yes
FOS	438	8.094637871	0.043106005	Yes
NR4A1	633	6.239775658	0.039072264	Yes
JUN	724	5.765926361	0.047315706	Yes
MAPK14	743	5.653651714	0.064058736	Yes
GATA3	773	5.489055157	0.079503216	Yes
NR3C1	807	5.352002144	0.09447549	Yes
ICAM1	842	5.218481064	0.10932973	Yes
SFN	1006	4.534712791	0.10895553	Yes
POU2F1	1229	3.750123978	0.1016164	Yes
STAT5B	1334	3.453756094	0.108207144	Yes
RELA	1463	3.156321526	0.11196469	Yes
CREBBP	1514	3.016171217	0.12493012	Yes
KMT5B	1591	2.888596058	0.13482626	Yes
SMARCC1	1637	2.803568363	0.14838195	Yes
VIPR1	1770	2.590506792	0.1516673	Yes
MAPK8	2006	2.241907597	0.14279352	Yes
AKT1	2131	2.077228785	0.14702326	Yes
SMARCC2	2200	1.983715415	0.1578638	Yes
PBX1	2251	1.92462647	0.17082924	Yes
NCOA1	2331	1.827400446	0.18037122	Yes
PRKACA	2559	1.603734374	0.17244184	Yes
EP300	2856	1.305983067	0.15636702	Yes
CREB1	2877	1.294376493	0.17287394	Yes
STAT5A	3036	1.15143168	0.17309	Yes
HSP90AA1	3142	1.076227903	0.1795627	Yes
FKBP4	3145	1.075295925	0.19819452	Yes
NCOA2	3206	1.041746736	0.20997946	Yes

Orange shading identifies genes associated with cell cycle, mitogenesis, apoptosis or tumor growth

Supplementary Table 2: Genes from WP_GLUCOCORTICOID_RECEPTOR_PATHWAY enriched in all cells*

SYMBOL	RANK IN GENE LIST	RANK METRIC SCORE	RUNNING ES	CORE ENRICHMENT
ALOX5AP	7	71.16706848	0.03288677	Yes
PTGS2	60	20.32308197	0.055513624	Yes
PDE4B	63	19.07024193	0.089540385	Yes
SRGN	250	1.820487499	0.081615485	Yes
ARL5B	325	0.782671869	0.09922638	Yes
CDC42EP3	361	0.512339413	0.1257292	Yes
BHLHE40	375	0.414142698	0.15724799	Yes
NR3C1	421	0.225954607	0.18147083	Yes
TNFAIP3	440	0.162032276	0.21184961	Yes
RGS2	603	0.003479103	0.20939668	Yes
CCL2	628	9.29E-04	0.23840748	Yes
SERTAD2	852	-0.065622799	0.22204664	Yes
GADD45B	905	-0.09557309	0.24467349	Yes
NFKB2	912	-0.101119801	0.27778825	Yes

Orange shading identifies genes associated with cell cycle, mitogenesis, apoptosis or tumor growth

*excluding seminal vesicle population

SUPPLEMENTARY FIGURE LEGENDS

Figure S1. Comparison of MR and HFUS imaging protocols in Hi-MYC GEMM. Hi-MYC mice (n=3) harboring tumors of varying size were imaged using both MR and HFUS imaging protocols, as previously described (6, 19), to assess tumor volume. Representative images from MR (**A**) and HFUS (**B**) imaging protocols. **C.** Plot of tumor volumes determined by MR and HFUS imaging, demonstrating a high degree of correlation (r^2 = 0.99).

Figure S2. Intra-prostatic androstenedione (AD), dehydroepiandrosterone (DHEA) and androsterone (5α-dione) were undetectable in PTEN-deficient mice. Tissue samples from the mice employed in Fig. 4 were further analyzed for testosterone and dihydrotestosterone precursors (shown in red, in **A**), as described in the **Materials and Methods**. **A.** Partial scheme of androgen biosynthesis adapted from Sharifi (33). Abbreviations and the corresponding trivial names are shown in the inset. **B-D**, Levels of the androgen precursors androstenedione, androsterone and dehydroepiandrosterone were undetectable in pre- and post-castration prostate cancer tissue samples.

Figure S3. An inhibitor of glucocorticoid signaling blocks castration-induced delayed regression: plots of individual mice corresponding to Figures 5B and 6B. A. Relative tumor volume of PB-Cre4:Pten$^{fl/fl}$ mice castrated and treated with/without CORT12528, as per Figure 5. Uppermost panel is a reproduction of Figure 5B (median +/-SE) ; the middle panel shows plots for individual castrated mice treated with CORT12528; and the bottom panel shows plots for individual castrated mice. **B.** Relative tumor volume of ARR_2/PB-*Myc* mice castrated and treated with/without CORT12528, as per Figure 6. Uppermost panel is a reproduction of Figure 6B (median, +/- SE) ; the middle panel shows plots for individual castrated mice treated with CORT12528; and the bottom panel shows plots for individual castrated mice.

Figure S4. Complete immunoblot images corresponding to Figure 7. A-D. Immunoblots prepared using lysates from Hi-MYC GEMM (corresponding to Fig. 7B). **E-F.** Immunoblots prepared using lysates from PTEN-deficient GEMM (corresponding to Fig. 7A). Based on multiple publications and the mass markers, the full-length GR and AR proteins were identified as the slowest migrating band visible on the immunoblot image, as indicated.

Figure S5. GR-transcript counts from scRNAseq data sets, corresponding to Figure 8C. Box plots of transcript counts corresponding to all GR-expressing cells (GR+ cells; left side) and in GR-expressing epithelial tumor cells (GR+ epithelial cells; right side), as identified in Figure 8A-B. The lower panels show the same data, with pooling of identically treated sets of mice. T-tests were performed on the pooled data and the p-values indicated in the figure.

Figure S6. Extended data from differential gene expression and gene set enrichment analysis, corresponding to Figure 8D. Differential gene expression of the pooled transcripts from 'All cells' (excluding the seminal vesicle population) (A) and from the epithelial cell population only (B), followed by GSEA identified one glucocorticoid signaling gene set (PID_REG_GR_PATHWAY) that was significantly upregulated in the epithelial cell population. Genes with low variance and low expression across samples were removed before downstream analysis. **A.** All cells. Out of 17813 genes, 4417 genes (24.8%) were used to perform DEG across the entire cell population shown in Fig. 8A (excluding seminal vesicle). Among GR-related gene sets, only WP_GLUCOCORTICOID_RECEPTOR_PATHWAY was significantly upregulated in the 4d castrated group. **B.** Epithelial (tumor) cells only. Out of 17813 genes, we kept 8524 genes (47.9%) were used to perform DEG across the epithelial cell population shown in Fig. 8A. PID_REG_GR_ PATHWAY was significantly upregulated in castrated group. The enrichment plot is also shown in Fig. 8D.

FIGURE S1

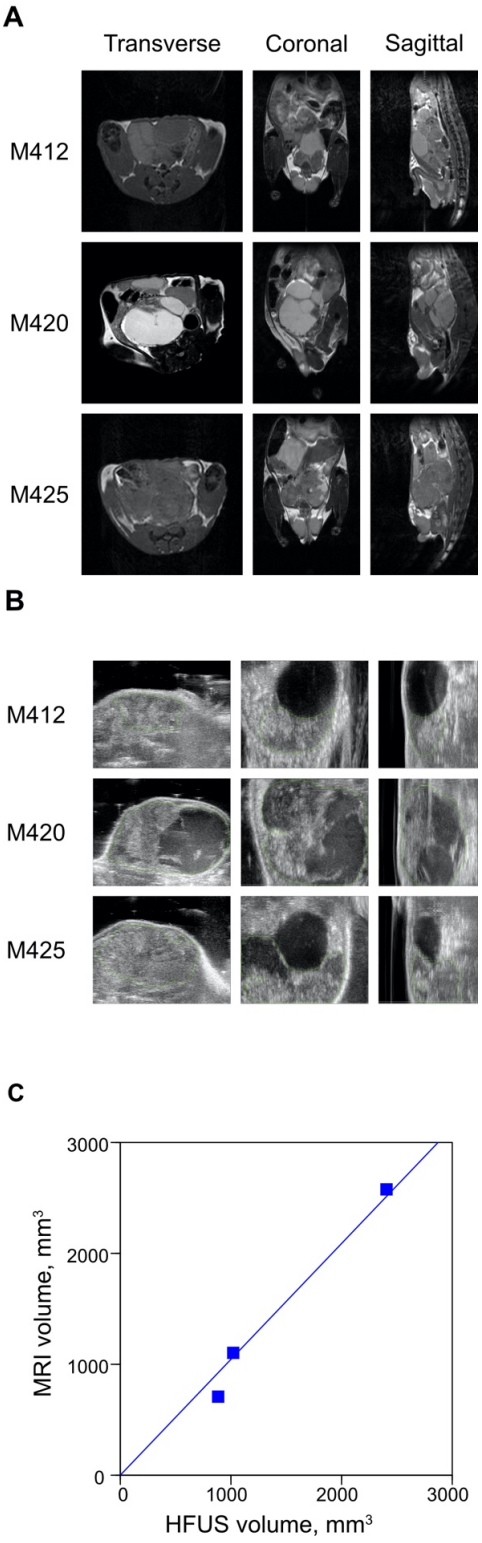
A
Transverse
Coronal
Sagittal
M412
M420
M425
B
M412
M420
M425
C
MRI volume, mm3
HFUS volume, mm3
0
1000
2000
3000

FIGURE S2

A

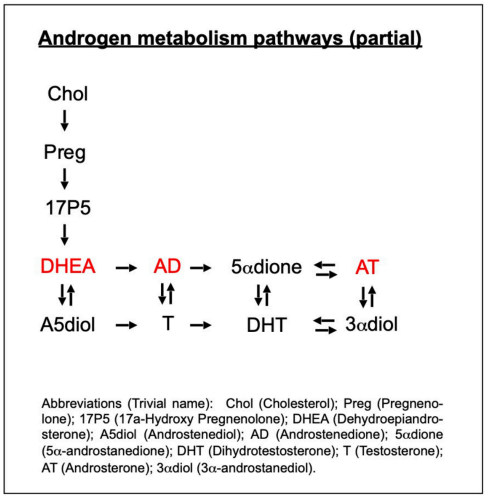

B

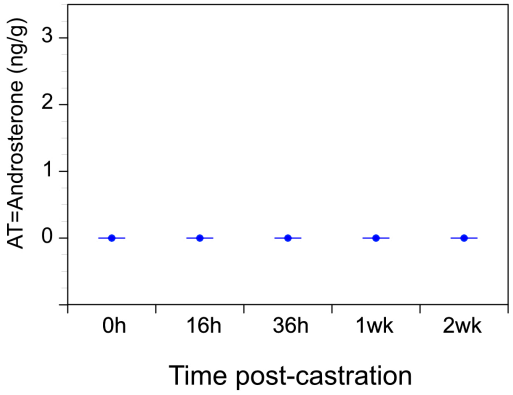

C

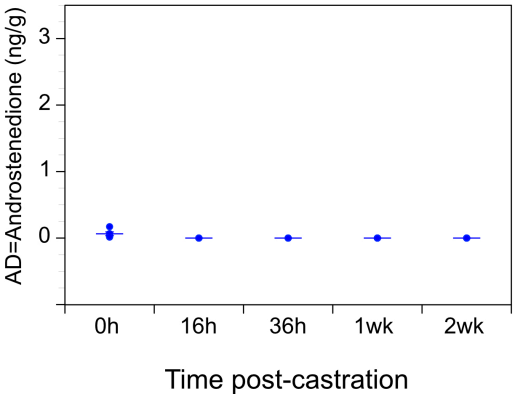

D

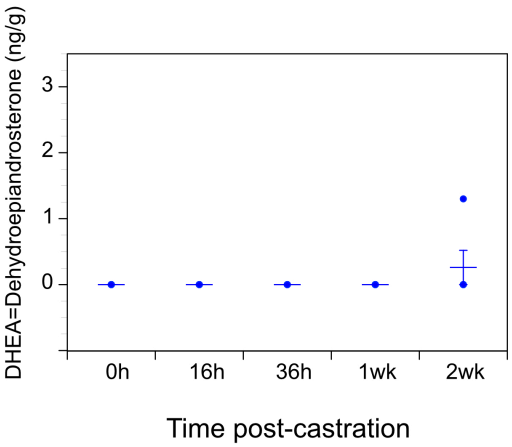

FIGURE S3

A - PTEN-deficient mice:

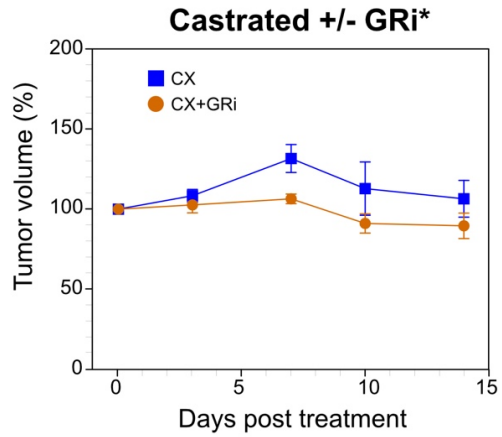

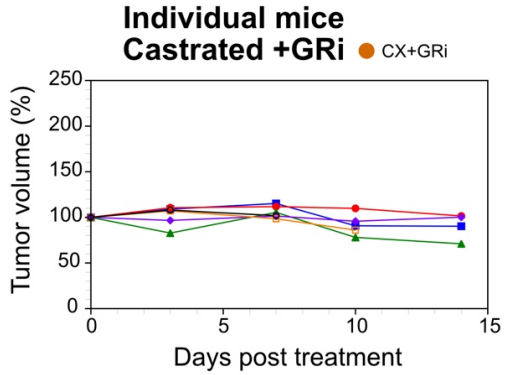

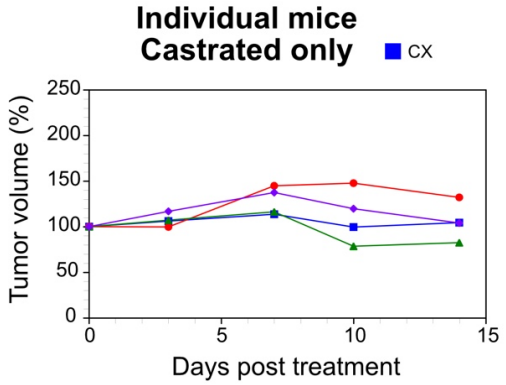

*Reproduced from Fig. 5C

B - Hi-MYC mice:

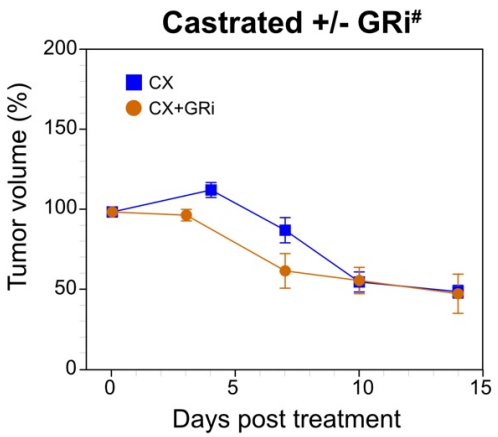

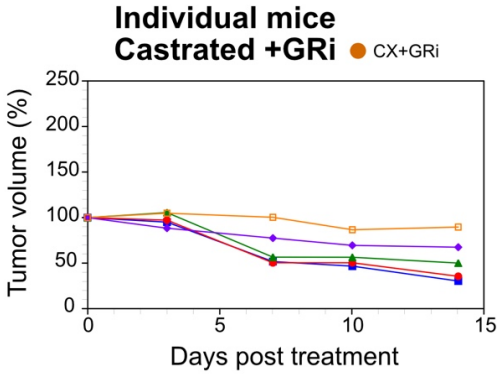

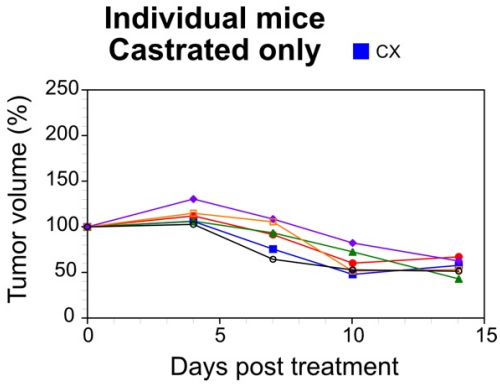

#Reproduced from Fig. 6D

FIGURE S4

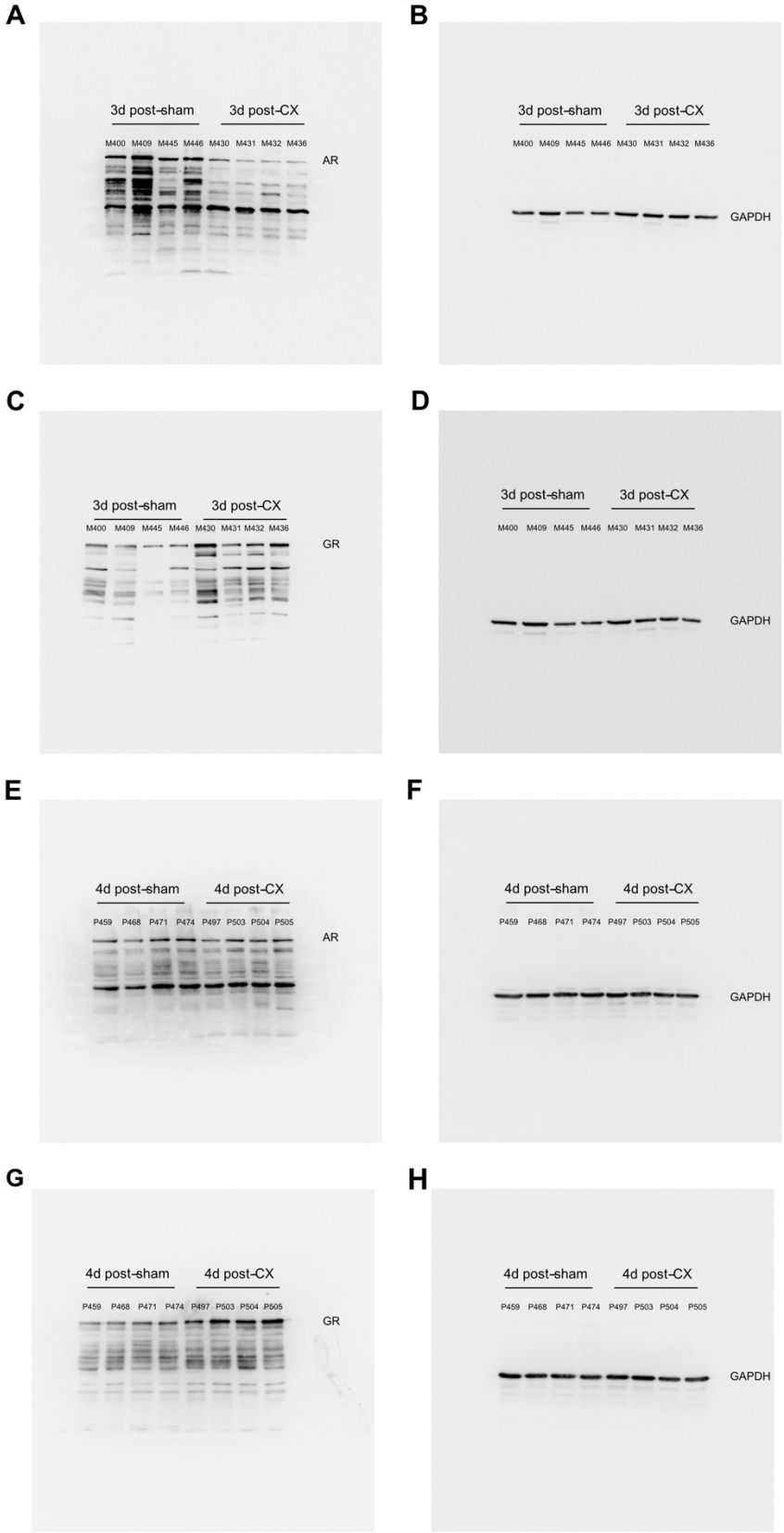
A
3d post-sham
3d post-CX
M400 M409 M445 M446 M430 M431 M432 M436
AR
B
3d post-sham
3d post-CX
M400 M409 M445 M446 M430 M431 M432 M436
GAPDH
C
3d post-sham
3d post-CX
M400 M409 M445 M446 M430 M431 M432 M436
GR
D
3d post-sham
3d post-CX
M400 M409 M445 M446 M430 M431 M432 M436
GAPDH
E
4d post-sham
4d post-CX
P459 P468 P471 P474 P497 P503 P504 P505
AR
F
4d post-sham
4d post-CX
P459 P468 P471 P474 P497 P503 P504 P505
GAPDH
G
4d post-sham
4d post-CX
P459 P468 P471 P474 P497 P503 P504 P505
GR
H
4d post-sham
4d post-CX
P459 P468 P471 P474 P497 P503 P504 P505
GAPDH

FIGURE S5

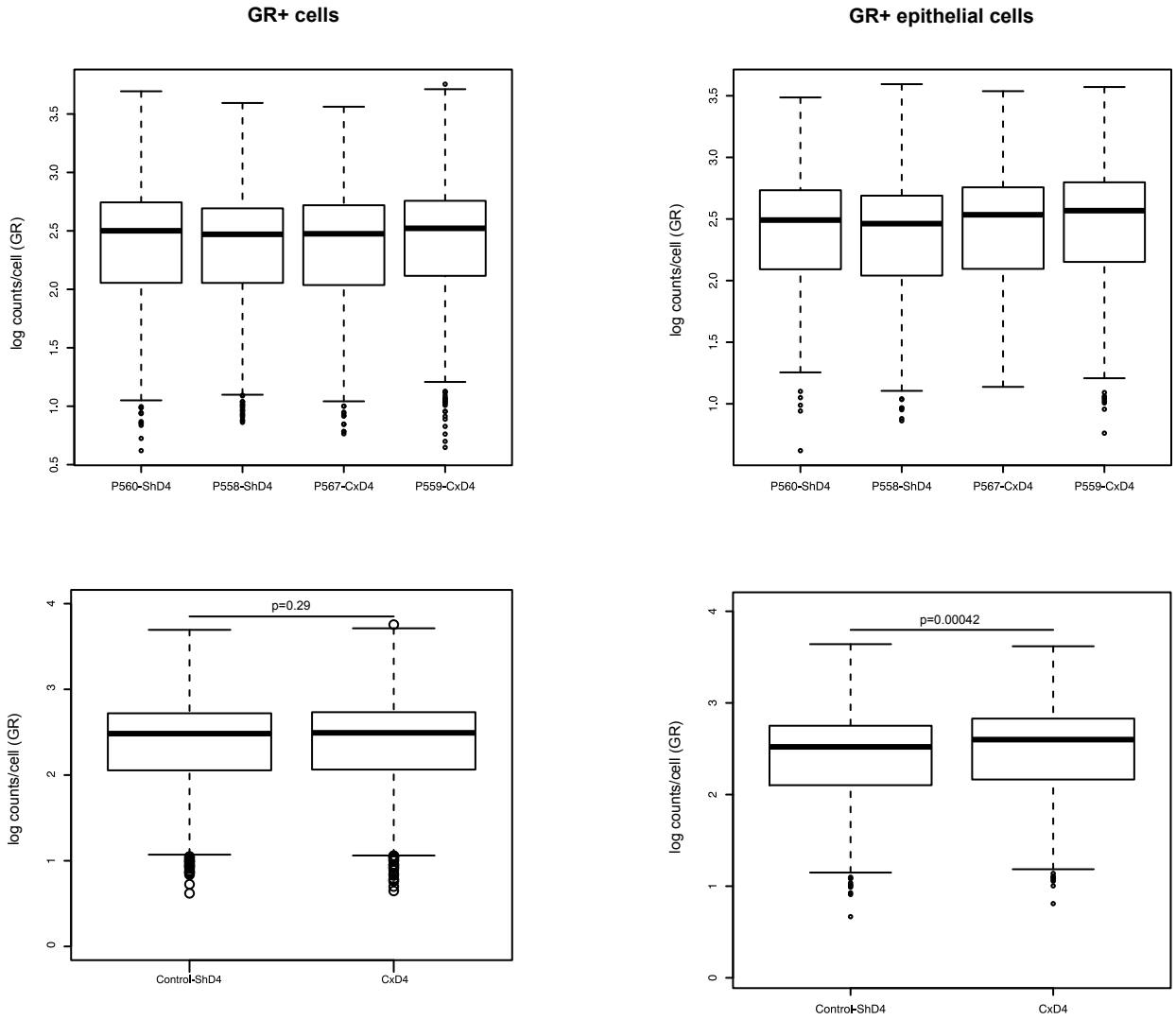
GR+ cells
GR+ epithelial cells
log counts/cell (GR)
P560-ShD4
P558-ShD4
P567-CxD4
P559-CxD4
p=0.29
p=0.00042
Control-ShD4
CxD4

FIGURE S6

A

All cells*

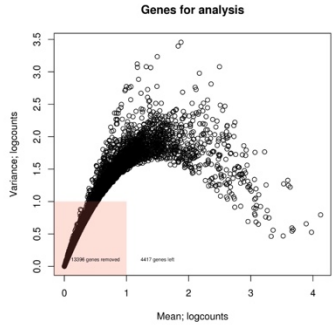

Low variance low expression genes were removed.
Cut-off: Variance<1; Mean<1

Total genes: 17813
Genes removed: 13396
Genes left for GSEA analysis: 4417

* Except 'Seminal Vesicle Epithelial' cluster

Correction: MA scRNAseq GR pathways GSEA analysis summary 20210810 RZ

All cells* (Up-regulated):
WP_GLUCOCORTICOID_RECEPTOR_PATHWAY

Dataset	20210806 GSEA.ranked.list.MA.Cx4dvsSham4d
Phenotype	NoPhenotypeAvailable
Upregulated in class	na_pos
GeneSet	WP_GLUCOCORTICOID_RECEPTOR_PATHWAY
Enrichment Score (ES)	0.27778825
Normalized Enrichment Score (NES)	1.7574453
Nominal p-value	0.027813413
FDR q-value	0.05663246
FWER p-Value	0.042

Standard name	WP_GLUCOCORTICOID_RECEPTOR_PATHWAY
Systematic name	M40042
Brief description	Glucocorticoid Receptor Pathway
Full description or abstract	
Collection	C2: curated gene sets CP: canonical pathways CP:WIKIPATHWAYS: WikiPathways gene sets
Source publication	
Exact source	WP2880
Related gene sets	
External links	http://www.wikipathways.org/instance/WP2880_r112288
Filtered by similarity	
Organism	Homo sapiens
Contributed by	WikiPathways
Source platform	Human_NCBI_Gene_ID

https://www.gsea-msigdb.org/gsea/msigdb/cards/WP_GLUCOCORTICOID_RECEPTOR_PATHWAY.html

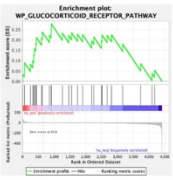

* Except 'Seminal Vesicle Epithelial' cluster
Cut-off: p-value < 0.05; FDR < 0.25

B

Epithelial cells

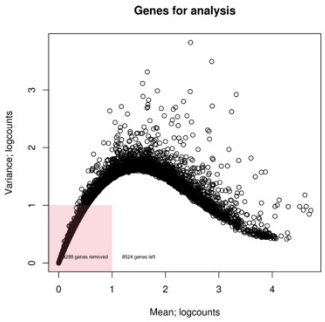

Low variance low expression genes were removed.
Cut-off: Variance<1; Mean<1

Total genes: 17813
Genes removed: 9289
Genes left for GSEA analysis: 8524

Correction: MA scRNAseq GR pathways GSEA analysis summary 20210810 RZ

Epithelial cells (Up-regulated):
PID_REG_GR_PATHWAY

Dataset	20210810 Epithelial GSEA.ranked.list.MA.Cx4dvsSham4d
Phenotype	NoPhenotypeAvailable
Upregulated in class	na_pos
GeneSet	PID_REG_GR_PATHWAY
Enrichment Score (ES)	0.20997946
Normalized Enrichment Score (NES)	1.7836622
Nominal p-value	0.017964079
FDR q-value	0.041802976
FWER p-Value	0.033

Standard name	PID_REG_GR_PATHWAY
Systematic name	M115
Brief description	Glucocorticoid receptor regulatory network
Full description or abstract	
Collection	C2: curated gene sets CP: canonical pathways CP:PID: PID gene sets
Source publication	Pubmed 18832364 Authors: Schaefer CF,Anthony K,Krupa S,Buchoff J,Day M,Hannay T,Buetow KH
Exact source	
Related gene sets	(show 195 additional gene sets from the source publication)
External links	
Filtered by similarity	
Organism	Homo sapiens
Contributed by	Pathway Interaction Database (NCI, NIH and Nature Publishing Group)
Source platform	Human_UniProt_ID

https://www.gsea-msigdb.org/gsea/msigdb/cards/PID_REG_GR_PATHWAY

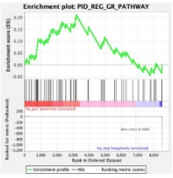

Cut-off: p-value < 0.05; FDR < 0.25